

Prediction of traffic oscillation instability with spectral analysis of the Aw–Rascle–Zhang model

Francois Belletti, Mandy Huo, Xavier Litrico, Alexandre M. Bayen^a

^aaddress

Abstract

This article starts from the classical Aw-Rascle-Zhang (ARZ) model for freeway traffic and develops a spectral analysis of its linearized version. A counterpart to the Froude number in hydrodynamics is defined that enables a classification of the nature of vehicle traffic flow using the explicit solution resulting from the analysis. We prove that our linearization about an equilibrium is stable for congested regimes and unstable otherwise. NGSIM data for congested traffic trajectories is used so as to confront the linearized model's predictions to actual macroscopic behavior of traffic. The model is shown to achieve good accuracy for speed and flow. In particular, it replicates the propagation of boundary conditions' oscillations into the interior resolution domain of the PDE under study.

Keywords: Second order models, Aw-Rascle-Zhang, Spectral Analysis, Linear Systems, Linearization of PDEs

1. Introduction

As personal vehicle ownership increases globally, traffic congestion continues to be a persistent problem. The goal of this research on physics of traffic is to gain a better understanding of the dynamics core to the system so as to design proper control techniques that can be applied to any road section. Strategies such as ramp metering and variable speed limits are in place today, but improved models of traffic dynamics could lay the foundations for more efficient coordination of such actuators.

What constitutes an “accurate” model often depends on the practitioners’ requirements. A model appropriate for a given application must describe key phenomena in the dynamics of the system under scrutiny so that they can be controlled efficiently. For traffic, a commonly used class of models relies on hydrodynamic theory, modeling vehicular flow in an aggregate manner. However, control schemes are only as reliable as the models on which they are based. Given that each model can only reproduce some features of traffic flow, one challenge of traffic engineering is the selection of the model most appropriate for the application of interest. We begin with a short summary of the history of models leading to the model of interest in this article.

1.1. First-order models

The 1950’s saw the development of the *Lighthill–Whitham–Richards* (LWR) model [1, 2], which became the seminal model for aggregate traffic flow. In this framework, the dynamics of this first-order scalar hyperbolic conservation law is governed by

$$\rho_t + (Q(\rho))_x = 0, \quad (1)$$

where ρ is the lineic vehicular density (veh/m), and $Q(\rho)$ is the empirically measured traffic flux (veh/s), also referred to as the fundamental diagram. Numerous phenomenological models exist for $Q(\rho)$, such as the Greenshields model [3], the Greenberg model [4], the triangular model, [5, 6], exponential models, [7, 8, 9] and many others [10, 11]. The simplicity of the LWR model enabled the formulation of numerical discretization schemes such as the Godunov scheme [12, 13], later renamed the cell transmission model [6, 14] in the transportation community.

However, first-order models have inherent shortcomings, most of which are discussed at length in [15], such as the failure to capture accurately shock structure, light traffic dynamics, and stop-and-go behavior,

otherwise known as traffic oscillations. Oscillations have attracted increasing attention in transportation research. For example jamitons, traffic jams that appear without the presence of a bottleneck, have been reproduced in contained experiments [16, 17] and explained theoretically as the result of both particular configurations of the traffic system [9] and fuzzy fundamental diagrams [18].

1.2. First-generation second-order models

In an effort to refine traffic modeling, Payne and Whitham followed the same approach as in fluid dynamics, developing a higher-order model to capture momentum-related features [19, 20]. The *Payne–Whitham* (PW) model consists of a mass conservation equation as in the LWR model,

$$\rho_t + (\rho v)_x = 0, \quad (2)$$

where ρ and v are the density and velocity, respectively. This is seconded by a momentum equation,

$$v_t + vv_x + \frac{p'(\rho)}{\rho} \rho_x = \frac{V(\rho) - v}{\tau} + \nu v_{xx}, \quad (3)$$

where the pressure function, $p(\rho)$, is strictly increasing and the equilibrium speed, $V(\rho)$, is nonincreasing. Both are empirically measured and $V(\rho)$ satisfies $Q(\rho) = \rho V(\rho)$. The parameters τ and ν are nonnegative, representing the relaxation time and coefficient of viscosity, respectively. This approach, however, has issues in both the derivation of its equations, and its predictions [15]. The PW model relies on the assumption that spacing and speed vary slowly, yielding negligible second and third derivatives for these quantities. This is contradictory with the observations of Newell [21] given that the car-following model predicts sharp changes in these quantities. Moreover, the PW model violates the anisotropy of traffic flow and can predict negative speeds if $\nu \neq 0$ [22].

1.3. Second-generation second-order models

Despite the criticism expressed in [15] regarding higher-order models inspired by fluid dynamics, Zhang proposed improved models to resolve issues plaguing earlier second-order models. In [23], he proposed a modification of the momentum equation of the PW model to handle the issue of backward-propagating traffic. Soon after, Aw and Rascle [24] presented a model with the following momentum equation:

$$(v + p(\rho))_t + v(v + p(\rho))_x = \frac{V(\rho) - v}{\tau}. \quad (4)$$

Including the pressure term, $p(\rho)$, in a convective derivative guarantees that no information travels faster than the speed of the cars. Aw and Rascle demonstrated in [24] that “with a suitable choice of function p ,” the above class of models avoids inconsistencies of earlier second-order models. Zhang proposed in [22] the same model with $p(\rho) = -V(\rho)$. With this choice of $p(\rho)$, the model is referred to as the *Aw–Rascle–Zhang* (ARZ) model, which is the model used in the present article.

This model has since been thoroughly studied. The work in [24] concluded that a relaxation term accounting for traffic equilibrium was needed so the speed of cars would be determined by the fundamental diagram and not the initial data. Rascle later proved in [25] that the relaxed model converges towards the LWR model as $\tau \rightarrow 0$. The first ARZ model requires a fundamental diagram extended to negative and maximum speeds, and zero and maximum densities so as to guarantee solutions to the Riemann problem and stability with low densities [26]. In [27], discretization enabled extension of the AR model to a network setup with junctions and traffic lights, detailed solutions for Riemann problems at junctions are presented in [28]. With an extended fundamental diagram, any Riemann problem for the ARZ model can be solved, allowing for a Godunov discretization scheme and numerical comparison in which the ARZ model fits real data better than the LWR model [29].

More recently a generalized model proposed in [30] corrects the fact that, in the ARZ model, several maximum densities co-exist, seemingly contradictory to the intuition that this quantity is uniquely determined by the characteristics of the freeway. Although more realistic, such a model does not allow proper linearization about an equilibrium, a procedure core key to making second-order models more tractable.

1.4. Models appropriate for control

As mentioned in [30], for congested regimes, the LWR model tends to offer a slightly better fit than the ARZ model with respect to empirical measurements but is outperformed for low densities. For predictions, we could use different models and switch to the one most adapted to the traffic conditions we observe. However, our aim is to design a robust model that paves the way to designing generic control strategies readily usable in all traffic conditions. Therefore we use instead the ARZ model linearized around arbitrary nominal conditions.

Laplace transform and spectral analysis are powerful tools for control problems, providing a simple yet holistic representation of a system. In this regard, it is important to have a model that predicts oscillatory phenomena. Specific classes of second-order models, including the ARZ model, realistically account for traffic oscillations in dense traffic [31]. Behavioral models such as in [21], and more recently [32], depict in a detailed fashion the effects of car-following and lane-changing on freeway dynamics, effects often cited as the cause of oscillations [33, 34, 35]. However, second-order macroscopic models are most suited for our method.

Fourier and Laplace transforms are not the only spectral operators useful for studying traffic. Approaches such as [36] attempt to model spectral features of traffic using wavelets to account for turbulent phenomena on various time scales. The method presented here differs in that it is driven mostly by macroscopic physics rather than data analysis.

1.5. Similarities with Saint-Venant equations

Our control analysis of the ARZ equations is strongly inspired by the pioneering analysis of Litrico and Fromion for the Saint-Venant equations, see in particular the monograph [37]. The Saint-Venant equations are as follows:

$$Ty_t + q_x = 0, \quad (5)$$

$$v_t + vv_x + gy_x = g(S_b - S_f), \quad (6)$$

where v is the fluid velocity in a canal, q the flux, T the top width, y the water height, S_f the friction slope, and S_b the bed slope. Note the structural similarity to the ARZ equations. In the equilibrium regime, the term $S_b - S_f(x, t)$ is zero under uniform flow, making it analogous to the relaxation term $\frac{V(\rho) - v}{\tau}$, designed to be zero at the equilibrium. Linearizing this system around an equilibrium point enables the use of spectral methods to design efficient control strategies for canals [38] thus allowing hydrodynamicists to implement control theory effectively. Approximations for the low frequency domain decompose the transfer matrix into a combination of delay and integration components, allowing for design of efficient PI and H_∞ controllers while enabling a simpler theoretical analysis of hydraulic systems [37, 38].

1.6. Approach and contributions

The present article extends the corresponding spectral framework of [37] to the case of the ARZ equations so as to achieve a two-fold objective:

- We aim to develop strategies that enforce ease of use of the ARZ model for stability analysis and control. Analytical solutions to these non-linear equations are difficult to derive but linearization facilitates design of efficient control schemes with multiple inputs and outputs. We pay particular attention to the formulation of boundary conditions, to guarantee the well-posedness of the problem.
- We assess the quality of the model by comparing its output with actual data collected in the field (using the NGSIM dataset).

The contributions of this article are as follows:

- *Modeling:* We derive the characteristic form by linearization and diagonalization of the ARZ model. This form highlights important features of the model, leading to the definition of a counterpart to the Froude number in hydrodynamics [37], which separates free-flow and congested regimes. This is carried out in the (ρ, v) , (ρ, q) , and (v, q) form, which can all be used interchangeably depending on applications. For example, in case when only v and q are measured (such as GPS and loops), the (v, q) version of the equation is very appropriate to use.

- *Spectral analysis:* From the characteristic form we derive the spectral form: a distributed transfer function [37]. Time domain responses derived from the spectral transfer matrices show that the linearized system is unstable in the free-flow regime. These waves occur for an entire set of values of velocity, density, and flux and lead the linearized system away from its equilibrium point in the free-flow regime.
- *Numerical validation:* A numerical experiment using NGSIM data is conducted to verify that linearization does not destroy realistic properties of the ARZ model. Previous studies also using NGSIM data to assess predictions of second-order models focused on averaged errors and only displayed predictions at a couple of points along the freeway [29, 30]. Here, we present an entire map of the states and conduct model assessment in a holistic manner, providing a complete analysis of the strengths and weaknesses of the model to be used for control. Our estimation procedure, unlike [30], does not rely on any assumption about the typical vehicle length or the safety distance factor. Additionally, no discretization scheme is needed and no grid size condition needs to be fulfilled. This procedure demonstrates that the linearized model successfully accounts for traffic oscillations and also provides simple and consistent methods to calibrate the relaxation time, τ .

1.7. Organization of the article

The rest of this article is organized as follows. In Section 2 we present the characteristic form of the ARZ model in several state variables, leading to the derivation of the spectral form of the flux and velocity system in section 3. We focus on these states in particular as they are the most easily observed and controlled in traffic. Properties of the spectral form in the two flow regimes are also analyzed. Section 4 focuses on numerical analysis. We present estimation procedures for (v, q, ρ) and the model parameters, comparing empirical estimates with numerical predictions of the linearized model. Finally, we use *Fast Fourier Transform* (FFT) to turn the spectral model into a numerical prediction tool.

2. The ARZ model

We consider the ARZ model with relaxation term. The model is shown here:

$$\rho_t + (\rho v)_x = 0, \quad (7)$$

$$(v - V(\rho))_t + v(v - V(\rho))_x = \frac{V(\rho) - v}{\tau}, \quad (8)$$

where ρ is the density, v is the velocity, τ is the relaxation time, and $V(\rho) = Q(\rho)/\rho$ is the equilibrium velocity profile, where $Q(\rho)$ is the density-flow relation given by the fundamental diagram. We assume that V is C^1 derivable over its domain. Without the relaxation term cars never reach the maximum allowable speed [25]. Note that at the equilibrium velocity this term is zero.

In vector form the ARZ model is

$$\begin{pmatrix} \rho \\ v \end{pmatrix}_t + \begin{pmatrix} v & \rho \\ 0 & v + \rho V'(\rho) \end{pmatrix} \begin{pmatrix} \rho \\ v \end{pmatrix}_x = \begin{pmatrix} 0 \\ \frac{V(\rho) - v}{\tau} \end{pmatrix}. \quad (9)$$

With the appropriate variable change, we can rewrite the model in the density-flow and velocity-flow forms, the latter of which is most useful to us for practical control purposes. Using the flow relation $q = \rho v$ and (9), the density-flow form is

$$\begin{pmatrix} \rho \\ q \end{pmatrix}_t + \begin{pmatrix} 0 & 1 \\ -\frac{q}{\rho} \left(\frac{q}{\rho} + \rho V'(\rho) \right) & 2\frac{q}{\rho} + \rho V'(\rho) \end{pmatrix} \begin{pmatrix} \rho \\ q \end{pmatrix}_x = \begin{pmatrix} 0 & 0 \\ \frac{V(\rho)}{\tau} & -\frac{1}{\tau} \end{pmatrix} \begin{pmatrix} \rho \\ q \end{pmatrix}. \quad (10)$$

In the same manner we arrive at the velocity-flow form,

$$\begin{pmatrix} v \\ q \end{pmatrix}_t + \begin{pmatrix} v + \frac{q}{\rho} V' \left(\frac{q}{\rho} \right) & 0 \\ \frac{q}{v} \left(v + \frac{q}{\rho} V' \left(\frac{q}{\rho} \right) \right) & v \end{pmatrix} \begin{pmatrix} v \\ q \end{pmatrix}_x = \frac{1}{\tau} \begin{pmatrix} V \left(\frac{q}{\rho} \right) - v \\ Q \left(\frac{q}{\rho} \right) - q \end{pmatrix}. \quad (11)$$

Although the (ρ, q) and (v, q) forms are less common in transportation engineering, they bear interesting similarities to hydrodynamical systems. Moreover, they are promising for sensing problems as loop detectors typically sense (ρ, q) while GPS measurement generally yield estimates for v .

2.1. Linearization

We are interested in small deviations, $(\tilde{\rho}(x, t), \tilde{v}(x, t))$, from a given nominal profile. Consider the nominal solution $(\rho^*(x), v^*(x))(V(\rho^*) = v^*)$ satisfying $v_t = \rho_t = 0$. Then (9) becomes

$$v^* \rho_x^* + v_x^* \rho^* = 0, \quad (12)$$

$$(v^* + \rho^* V'(\rho^*)) v_x^* = \frac{V(\rho^*) - v^*}{\tau} = 0. \quad (13)$$

Then we must have $v_x^* = \rho_x^* = 0$, so the solution is uniform along the road.

Linearizing the ARZ model (9) around the nominal solution described above, we obtain

$$\begin{pmatrix} \tilde{\rho} \\ \tilde{v} \end{pmatrix}_t + \begin{pmatrix} v^* & \rho^* \\ 0 & v^* + \rho^* V'(\rho^*) \end{pmatrix} \begin{pmatrix} \tilde{\rho} \\ \tilde{v} \end{pmatrix}_x = \begin{pmatrix} 0 & 0 \\ \frac{V'(\rho^*)}{\tau} & -\frac{1}{\tau} \end{pmatrix} \begin{pmatrix} \tilde{\rho} \\ \tilde{v} \end{pmatrix}. \quad (14)$$

Similarly for the density-flow system (10), we linearize around the equilibrium $(\rho^*, q^*)(\rho^* V(\rho^*) = q^*)$ with deviations $(\tilde{\rho}(x, t), \tilde{q}(x, t))$. The linearized system is as follows:

$$\begin{pmatrix} \tilde{\rho} \\ \tilde{q} \end{pmatrix}_t + \begin{pmatrix} 0 & 1 \\ \alpha^* \beta^* & \alpha^* - \beta^* \end{pmatrix} \begin{pmatrix} \tilde{\rho} \\ \tilde{q} \end{pmatrix}_x = \begin{pmatrix} 0 & 0 \\ \delta & \sigma \end{pmatrix} \begin{pmatrix} \tilde{\rho} \\ \tilde{q} \end{pmatrix}, \quad (15)$$

where $\alpha^* = \frac{q^*}{\rho^*}$, $\beta^* = -\frac{q^*}{\rho^*} - \rho^* V'(\rho^*)$, $\delta = \frac{V(\rho^*) + \rho^* V'(\rho^*)}{\tau}$, and $\sigma = -\frac{1}{\tau}$.

Finally, for the velocity-flow system, we have

$$\begin{pmatrix} \tilde{v} \\ \tilde{q} \end{pmatrix}_t + \underbrace{\begin{pmatrix} v^* + \frac{q^*}{v^*} V' \left(\frac{q^*}{v^*} \right) & 0 \\ \frac{q^*}{v^*} \left(v^* + \frac{q^*}{v^*} V' \left(\frac{q^*}{v^*} \right) \right) & v^* \end{pmatrix}}_A \begin{pmatrix} \tilde{v} \\ \tilde{q} \end{pmatrix}_x = \underbrace{\begin{pmatrix} -\frac{(v^*)^2 + q^* V' \left(\frac{q^*}{v^*} \right)}{(v^*)^2 \tau} & \frac{V' \left(\frac{q^*}{v^*} \right)}{v^* \tau} \\ -\frac{q^* \left((v^*)^2 + q^* V' \left(\frac{q^*}{v^*} \right) \right)}{(v^*)^3 \tau} & \frac{q^* V' \left(\frac{q^*}{v^*} \right)}{(v^*)^2 \tau} \end{pmatrix}}_B \begin{pmatrix} \tilde{v} \\ \tilde{q} \end{pmatrix}. \quad (16)$$

2.2. Characteristic form

We diagonalize the linearized equations to obtain a more useful form of the model, which will then be treated in the spectral domain. We begin with the density-flow system. Standard algebraic manipulations of the equations in (14) lead to

$$\begin{pmatrix} \zeta_1 \\ \zeta_2 \end{pmatrix}_t + \begin{pmatrix} \lambda_1 & 0 \\ 0 & \lambda_2 \end{pmatrix} \begin{pmatrix} \zeta_1 \\ \zeta_2 \end{pmatrix}_x = \begin{pmatrix} -\frac{1}{\tau} & 0 \\ -\frac{1}{\tau} & 0 \end{pmatrix} \begin{pmatrix} \zeta_1 \\ \zeta_2 \end{pmatrix}, \quad (17)$$

where $\zeta_1 = \tilde{v} - V'(\rho^*)\tilde{\rho}$ and $\zeta_2 = \tilde{v}$ are the Riemann invariants of the (ρ, v) system, and $\lambda_1 = v^*$ and $\lambda_2 = v^* + \rho^* V'(\rho^*)$ are the eigenvalues. Note that $V'(\rho^*) \leq 0$ so $\lambda_2 \leq \lambda_1 = v^*$. Therefore this is consistent with the physical dynamics of the system as no waves travel faster than the equilibrium vehicle speed.

We proceed in the same manner as above to diagonalize the (ρ, q) system (15). The diagonal form is

$$\begin{pmatrix} \chi_1 \\ \chi_2 \end{pmatrix}_t + \begin{pmatrix} \lambda_1 & 0 \\ 0 & \lambda_2 \end{pmatrix} \begin{pmatrix} \chi_1 \\ \chi_2 \end{pmatrix}_x = \begin{pmatrix} -\frac{1}{\tau} & 0 \\ -\frac{1}{\tau} & 0 \end{pmatrix} \begin{pmatrix} \chi_1 \\ \chi_2 \end{pmatrix}, \quad (18)$$

where $\chi_1 = -\lambda_2 \tilde{\rho} + \tilde{q}$ and $\chi_2 = -\lambda_1 \tilde{\rho} + \tilde{q}$ are the characteristic variables in the (ρ, q) system and the eigenvalues λ_1 and λ_2 are the same as in the density-velocity system due to the relation $q^* = \rho^* v^*$.

Diagonalization of the velocity-flow system is more involved. Letting $\eta(x, t) = (\tilde{v}, \tilde{q})^T$, we can rewrite (16) as

$$\eta_t + A\eta_x = B\eta. \quad (19)$$

The eigenvalues of A are $\lambda_1 = v^*$ and $\lambda_2 = v^* + \frac{q^*}{v^*} V' \left(\frac{q^*}{v^*} \right)$, consistent with the previous systems. Then A can be diagonalized as follows

$$A = XDX^{-1}, \quad (20)$$

$$X = \begin{pmatrix} 0 & \lambda_2 - \lambda_1 \\ 1 & \rho^* \lambda_2 \end{pmatrix}, \quad (21)$$

$$D = \begin{pmatrix} \lambda_1 & 0 \\ 0 & \lambda_2 \end{pmatrix}, \quad (22)$$

$$X^{-1} = \begin{pmatrix} \frac{\rho^* \lambda_2}{\lambda_1 - \lambda_2} & 1 \\ \frac{1}{\lambda_1 - \lambda_2} & 0 \end{pmatrix}. \quad (23)$$

Define $\gamma(x, t) := X\eta(x, t)$. Hence (19) can be rewritten as

$$\gamma_t + \begin{pmatrix} \lambda_1 & 0 \\ 0 & \lambda_2 \end{pmatrix} \gamma_x = \begin{pmatrix} -\frac{1}{\tau} & 0 \\ -\frac{1}{q^* \tau} & 0 \end{pmatrix} \gamma \quad (24)$$

where

$$\gamma = \begin{pmatrix} \frac{\rho^* \lambda_2}{\lambda_1 - \lambda_2} \tilde{v} + \tilde{q} \\ \frac{1}{\lambda_1 - \lambda_2} \tilde{v} \end{pmatrix}. \quad (25)$$

Let $\xi = (\xi_1, \xi_2)^T = (\chi_1, -q^* \chi_2)^T$. Then we have

$$\begin{pmatrix} \xi_1 \\ \xi_2 \end{pmatrix}_t + \begin{pmatrix} \lambda_1 & 0 \\ 0 & \lambda_2 \end{pmatrix} \begin{pmatrix} \xi_1 \\ \xi_2 \end{pmatrix}_x = \begin{pmatrix} -\frac{1}{\tau} & 0 \\ -\frac{1}{q^* \tau} & 0 \end{pmatrix} \begin{pmatrix} \xi_1 \\ \xi_2 \end{pmatrix}, \quad (26)$$

and

$$\begin{pmatrix} \xi_1 \\ \xi_2 \end{pmatrix} = \begin{pmatrix} \frac{\rho^* \lambda_2}{\lambda_1 - \lambda_2} \tilde{v} + \tilde{q} \\ \frac{1}{\lambda_1 - \lambda_2} \tilde{v} \end{pmatrix} = \begin{pmatrix} \frac{\rho^* \lambda_2}{\lambda_1 - \lambda_2} & 1 \\ \frac{\rho^* \lambda_1}{\lambda_1 - \lambda_2} & 0 \end{pmatrix} \begin{pmatrix} \tilde{v} \\ \tilde{q} \end{pmatrix} \quad (27)$$

2.3. The Traffic Froude Number

In fluid mechanics, the Froude number is a dimensionless number which delineates the boundary between flow regimes [39, 37]. Using the eigenvalues of the system in the characteristic form, we are able to define a useful counterpart to this number. Since $V(\rho)$ is nonincreasing function, we have $V'(\rho^*) \leq 0$. Assuming $V'(\rho^*) \neq 0$ there are two flow regimes: one in which $\lambda_1 \lambda_2 < 0$ and one characteristic line travels downstream whereas the other characteristic line travels upstream, and one in which $\lambda_1 \lambda_2 > 0$ and both characteristic lines travel downstream.

We define the *Traffic Froude Number* (TFN) as

$$F = \left| \frac{\rho^* V'(\rho^*)}{v^*} \right|. \quad (28)$$

Then we have

$$\begin{cases} F > 1 & \Rightarrow |\rho^* V'(\rho^*)| > v^* \Rightarrow \lambda_2 < 0 \\ F < 1 & \Rightarrow |\rho^* V'(\rho^*)| < v^* \Rightarrow \lambda_2 > 0 \end{cases}.$$

Note also that $\lambda_2 = v^* + \rho^* V'(\rho^*) = \frac{Q(\rho^*)}{\rho^*} + \frac{\rho^* Q'(\rho^*) - Q(\rho^*)}{\rho^*} = Q'(\rho^*)$. Hence the system is in free-flow when $F < 1$ and congestion when $F > 1$. In hydrodynamics these regimes are referred to as the subcritical and supercritical regimes, respectively [37]. The direction of characteristic lines is illustrated in Figure 1.

For traffic, the interpretation of the different regimes is somewhat different. Free flow regime corresponds to these situations where drivers are not slowed down by heavy traffic and go as fast as the desired speed. The congested regime arises when traffic is denser and, because too many cars are present on the same freeway section, drivers slow down and eventually form traffic jam.

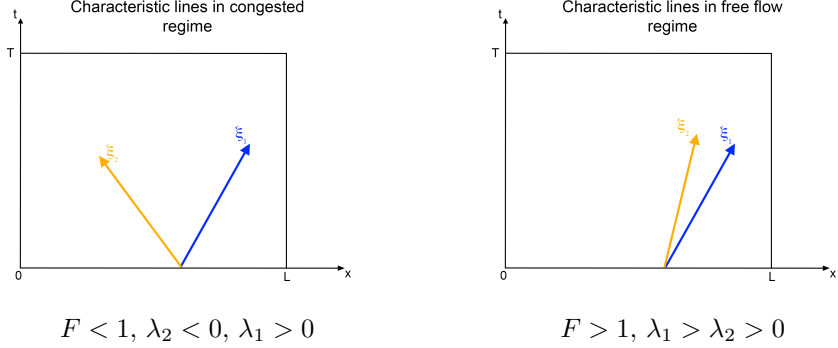


Figure 1: Illustration of characteristics in congested (supercritical) and free-flow regime (subcritical).

3. Spectral analysis of the linearized ARZ model

We now consider the (v, q) system for the frequency domain analysis for practical control purposes.

3.1. State-transition matrix

Taking the Laplace transform of the diagonalized form (26) we obtain

$$\frac{\partial \hat{\zeta}(x, s)}{\partial x} = \mathcal{A}(s)\hat{\zeta}(x, s) + \mathcal{B}\zeta(x, t=0^-), \quad (29)$$

where $\mathcal{A}(s) = A^{-1}(B - sI)$ and $\mathcal{B} = -A^{-1}$. The general solution to this ordinary differential equation is

$$\hat{\zeta}(x, s) = \Phi(x, s)\hat{\zeta}(0, s) + \Phi(x, s) \int_0^x \Phi(\nu, s)^{-1}\mathcal{B}\zeta(\nu, 0^-)d\nu, \quad (30)$$

where $\Phi(x, s) = e^{\mathcal{A}(s)x}$ is the state-transition matrix. Assuming zero initial conditions we have

$$\hat{\zeta}(x, s) = \Phi(x, s)\hat{\zeta}(0, s). \quad (31)$$

To compute the exponential we diagonalize the matrix as

$$\mathcal{A}(s) = \mathcal{X}(s)\mathcal{D}(s)\mathcal{X}^{-1}(s) \quad (32)$$

where

$$\mathcal{X}(s) = \begin{pmatrix} 0 & \frac{\lambda_2 - (\lambda_1 - \lambda_2)\tau s}{\lambda_1} \\ 1 & 1 \end{pmatrix}, \quad (33)$$

$$\mathcal{D}(s) = \begin{pmatrix} -\frac{s}{\lambda_2} & 0 \\ 0 & -\frac{1+\tau s}{\tau \lambda_1} \end{pmatrix}. \quad (34)$$

Hence

$$\Phi(x, s) = \mathcal{X}^{-1}(s)e^{\mathcal{D}(s)x}\mathcal{X}(s) = \begin{pmatrix} \phi_{11}(x, s) & \phi_{12}(x, s) \\ \phi_{21}(x, s) & \phi_{22}(x, s) \end{pmatrix}, \quad (35)$$

with

$$\phi_{11}(x, s) = e^{-\frac{x}{\tau \lambda_1}} e^{-\frac{x}{\lambda_1}s}, \quad (36a)$$

$$\phi_{12}(x, s) = 0, \quad (36b)$$

$$\phi_{21}(x, s) = \frac{\lambda_1 \left(e^{-\frac{x}{\tau \lambda_1}} e^{-\frac{x}{\lambda_1}s} - e^{-\frac{x}{\lambda_2}s} \right)}{\lambda_2 - \tau(\lambda_1 - \lambda_2)s}, \quad (36c)$$

$$\phi_{22}(x, s) = e^{-\frac{x}{\lambda_2}s}. \quad (36d)$$

Let $\alpha = -\frac{\lambda_2}{\tau(\lambda_1 - \lambda_2)}$. It is indeed clear that $\phi_{11}(x, s)$ decomposes as the product of a distributed delay corresponding to information propagating at speed λ_1 and attenuation proportional to $\frac{x}{\tau\lambda_1}$. Here $\tau\lambda_1$ plays the role of a characteristic spatial length. Similarly ϕ_{22} is a delay corresponding to information propagating at speed λ_2 . The interpretation of ϕ_{21} is more cumbersome. In low frequencies ($|s| \ll |\alpha|$), this transfer function takes a much more transparent form. Indeed, in the expression $\phi_{21}(x, s) = \frac{\lambda_1\alpha}{s+\alpha} e^{-\frac{x}{\lambda_2}s} \left(1 - e^{-\frac{x}{\lambda_1\tau}(s+\alpha)}\right) \simeq \frac{\lambda_1}{\lambda_2} e^{-\frac{x}{\lambda_2}s} \left(1 - e^{-\frac{x}{\lambda_1\tau}}\right)$ the transfer function appears as the combination of a distributed delay where λ_2 is the propagation speed and a gain where $\lambda_1\tau$ is a characteristic distance.

3.2. Free-flow case ($F < 1$)

Consider the system in the free-flow regime.

With $\zeta_1(0, t)$ and $\zeta_2(0, t)$ as the inputs and $\zeta_1(L, t)$ and $\zeta_2(L, t)$ as the outputs, the distributed transfer matrix is exactly the state-transition matrix $\Phi(x, s)$.

Using (27), we can write

$$\begin{pmatrix} \tilde{v}(x, s) \\ \tilde{q}(x, s) \end{pmatrix} = \underbrace{\begin{pmatrix} \frac{\rho^*\lambda_2}{\lambda_1 - \lambda_2} & 1 \\ \frac{\rho^*\lambda_1}{\lambda_1 - \lambda_2} & 0 \end{pmatrix}}_{\Psi(x, s)}^{-1} \Phi(x, s) \begin{pmatrix} \frac{\rho^*\lambda_2}{\lambda_1 - \lambda_2} & 1 \\ \frac{\rho^*\lambda_1}{\lambda_1 - \lambda_2} & 0 \end{pmatrix} \begin{pmatrix} \tilde{v}(0, s) \\ \tilde{q}(0, s) \end{pmatrix} \quad (37)$$

with

$$\psi_{11}(x, s) = \frac{\alpha e^{-\frac{x}{\lambda_1}(s+\frac{1}{\tau})} + s e^{-\frac{xs}{\lambda_2}}}{s + \alpha}, \quad (38a)$$

$$\psi_{12}(x, s) = -\frac{1}{\rho^*\tau} \frac{e^{-\frac{x}{\lambda_1}(s+\frac{1}{\tau})} - e^{-\frac{xs}{\lambda_2}}}{s + \alpha}, \quad (38b)$$

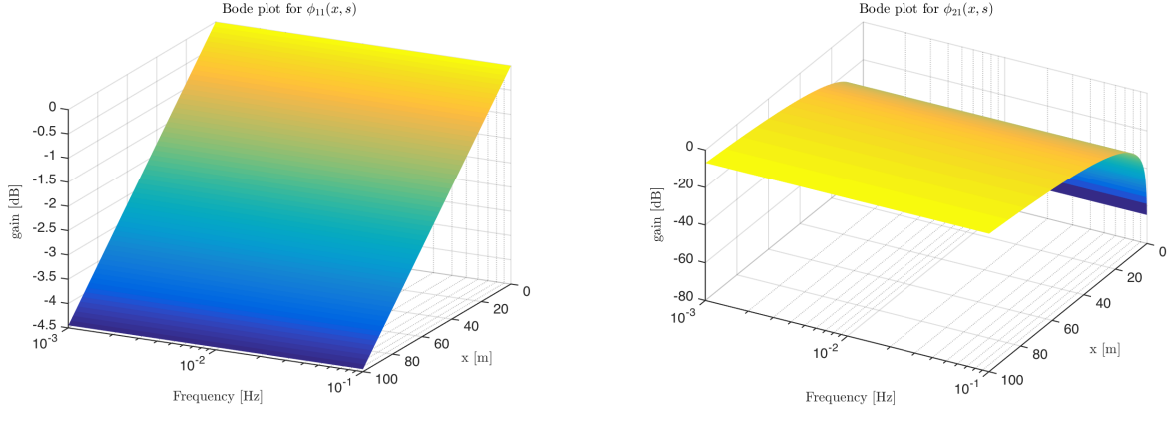
$$\psi_{21}(x, s) = -\rho^*\tau\alpha s \frac{e^{-\frac{x}{\lambda_1}(s+\frac{1}{\tau})} - e^{-\frac{xs}{\lambda_2}}}{s + \alpha}, \quad (38c)$$

$$\psi_{22}(x, s) = \frac{s e^{-\frac{x}{\lambda_1}(s+\frac{1}{\tau})} + \alpha e^{-\frac{xs}{\lambda_2}}}{s + \alpha}. \quad (38d)$$

It could appear at first sight that $-\alpha, > 0$, is a singularity of the transfer functions and therefore the system is not bounded-input/bounded-output stable. However, We have $\frac{1}{\lambda_1}(-\alpha + \frac{1}{\tau}) = \frac{1}{\tau(\lambda_1 - \lambda_2)} = \frac{-\alpha}{\lambda_2}$, thus a Taylor expansion about $-\alpha$ shows that numerators and denominators cancel each other out for $s \rightarrow -\alpha$ and $-\alpha$ is not a pole of any transfer function. This is enough to show that the output remains bounded for a given value of x . We will show below that a conic region of the $[0, T] \times [0, L]$ domain features exponential growth in free-flow regime. This arises when changing t and x simultaneously and complements the conclusion formulated with the spectral domain study (where t varies and x remains constant).

3.2.1. Low frequency approximation in free-flow regime

Analyzing the expressions above becomes easier when approximating them for $|s| \ll |\alpha|$. This is sensible concretely as one expects traffic related phenomena to occur at a low frequency. We find the following



Spatial magnitude Bode plot for $\phi_{11}(x, s)$.

Spatial magnitude Bode plot for $\phi_{21}(x, s)$.

Figure 2: Spatial magnitude Bode plots for Riemann invariants

approximate expressions for the transfer functions above:

$$\psi_{11}(x, s) = e^{-\frac{xs}{\lambda_2}} \frac{s + \alpha e^{-\frac{x}{\tau\lambda_1\alpha}(s+\alpha)}}{s + \alpha} \simeq e^{-\frac{xs}{\lambda_2}} e^{-\frac{x}{\tau\lambda_1}}, \quad (39a)$$

$$\psi_{12}(x, s) = \frac{e^{-\frac{xs}{\lambda_2}}}{\rho^* \tau} \frac{1 - e^{-\frac{x}{\tau\lambda_1\alpha}(s+\alpha)}}{s + \alpha} \simeq \frac{e^{-\frac{xs}{\lambda_2}}}{\rho^* \tau \alpha} \left(1 - e^{-\frac{x}{\tau\lambda_1}}\right), \quad (39b)$$

$$\psi_{21}(x, s) = s \rho^* \tau \alpha e^{-\frac{xs}{\lambda_2}} \frac{1 - e^{-\frac{x}{\tau\lambda_1\alpha}(s+\alpha)}}{s + \alpha} \simeq s \rho^* \tau e^{-\frac{xs}{\lambda_2}} \left(1 - e^{-\frac{x}{\tau\lambda_1}}\right), \quad (39c)$$

$$\psi_{22}(x, s) = e^{-\frac{xs}{\lambda_2}} \frac{\alpha + s e^{-\frac{x}{\tau\lambda_1\alpha}(s+\alpha)}}{s + \alpha} \simeq e^{-\frac{xs}{\lambda_2}}. \quad (39d)$$

Interpreting the low frequency expressions is fairly straightforward:

- In ψ_{11} , $e^{-\frac{xs}{\lambda_2}}$ is a distributed delay with propagation speed λ_2 and $e^{-\frac{x}{\tau\lambda_1}}$ a distributed gain with characteristic distance $\tau\lambda_1$.
- In ψ_{12} and ψ_{21} we can notice the combination of a distributed delay with characteristic speed λ_2 and a distributed gain with $\tau\lambda_1$ as a characteristic distance. It is also remarkable that $\tilde{q}(x, s)$ appears as the result of a derivation of $\tilde{v}(0, s)$.
- The approximate expression for ψ_{22} highlights the presence of a distributed delay where the information propagates at speed λ_2 .

3.2.2. Bode plots for free-flow regime

We generate Bode plots using the following parameters taken from [40]: $q_{\max} = 1300$ veh/h, $\rho_{\max} = 0.1$ veh/m, and $L = 100$ m. The Greenshields fundamental diagram, $Q(\rho) = 4\frac{q_{\max}}{\rho_{\max}^2} \rho(\rho_{\max} - \rho)$, is used to approximate the fundamental diagram. For inhomogeneous second-order models, the relaxation time, τ , falls in the range of about 14-60 seconds [30]. A relaxation time of $\tau = 15$ s is used for the following simulations. We simulate for $\rho^* = 0.01$ veh/m.

The Bode plots for the physical variables are displayed in Figures 4 and 5. For the Riemann invariants only $\phi_{21}(x, s)$ and $\phi_{22}(x, s)$ are represented in Figure 2 and Figure 3 ($\phi_{11}(x, s)$ and $\phi_{12}(x, s)$ are only delay functions).

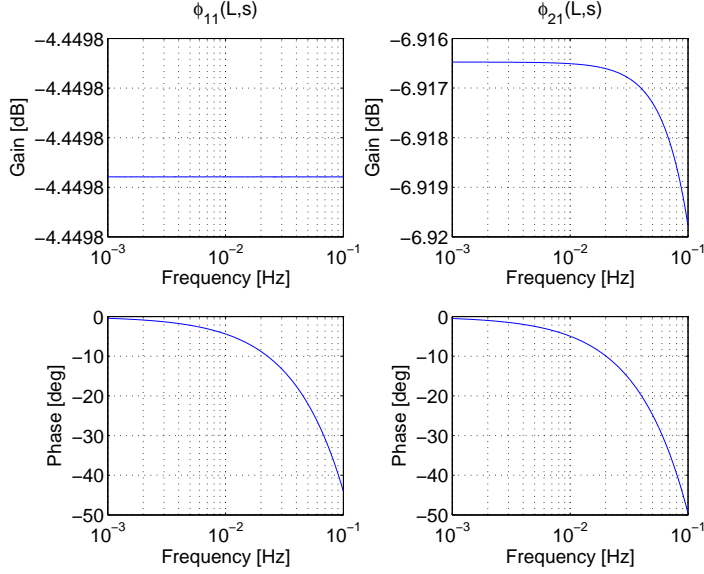


Figure 3: Magnitude and phase Bode plots for $\phi_{11}(L, s)$ and $\phi_{21}(L, s)$.

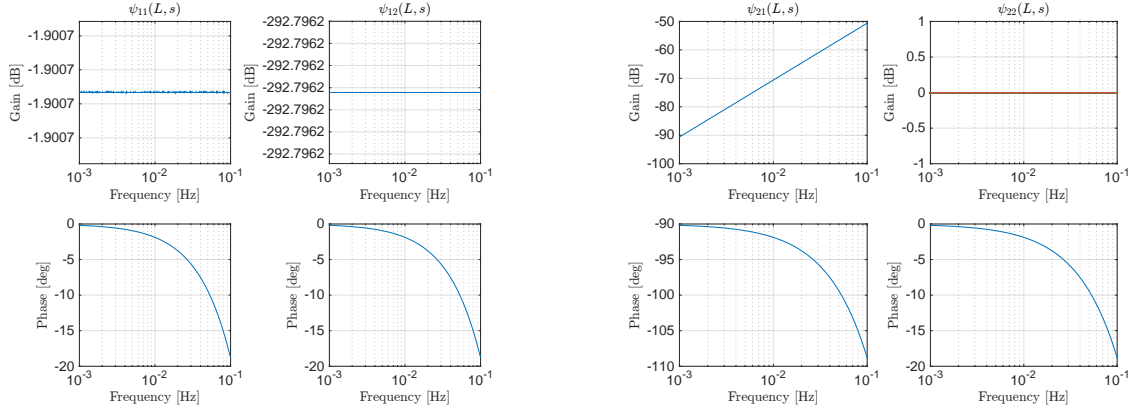


Figure 5: Magnitude and phase bode plots for $\psi_{11}(L, s)$ and $\psi_{12}(L, s)$ (left) and for $\psi_{21}(L, s)$ and $\psi_{22}(L, s)$ (right). (Physical variables).

3.2.3. Step responses

We analyze the behavior of the system given step inputs $v(0, t) = v_{\text{step}}H(t)$ and $q(0, t) = q_{\text{step}}H(t)$, where $H(\cdot)$ is the Heaviside function. The step responses can be explicitly computed from the spectral responses:

$$\begin{aligned} v(x, t) &= v_{\text{step}} \left[e^{-\frac{x}{\lambda_1 \tau}} H\left(t - \frac{x}{\lambda_1}\right) + e^{-\alpha(t - \frac{x}{\lambda_2})} \left(H\left(t - \frac{x}{\lambda_2}\right) - H\left(t - \frac{x}{\lambda_1}\right) \right) \right] \\ &\quad - \frac{q_{\text{step}}}{\rho^* \tau} \left[e^{-\frac{x}{\lambda_1 \tau}} H\left(t - \frac{x}{\lambda_1}\right) - H\left(t - \frac{x}{\lambda_2}\right) + e^{-\alpha(t - \frac{x}{\lambda_2})} \left(H\left(t - \frac{x}{\lambda_2}\right) - H\left(t - \frac{x}{\lambda_1}\right) \right) \right] \end{aligned} \quad (40)$$

$$\begin{aligned} q(x, t) &= v_{\text{step}} \rho^* \tau \alpha e^{-\alpha(t - \frac{x}{\lambda_2})} \left(H\left(t - \frac{x}{\lambda_1}\right) - H\left(t - \frac{x}{\lambda_2}\right) \right) \\ &\quad + q_{\text{step}} \left[H\left(t - \frac{x}{\lambda_2}\right) + e^{-\alpha(t - \frac{x}{\lambda_2})} \left(H\left(t - \frac{x}{\lambda_1}\right) - H\left(t - \frac{x}{\lambda_2}\right) \right) \right] \end{aligned} \quad (41)$$

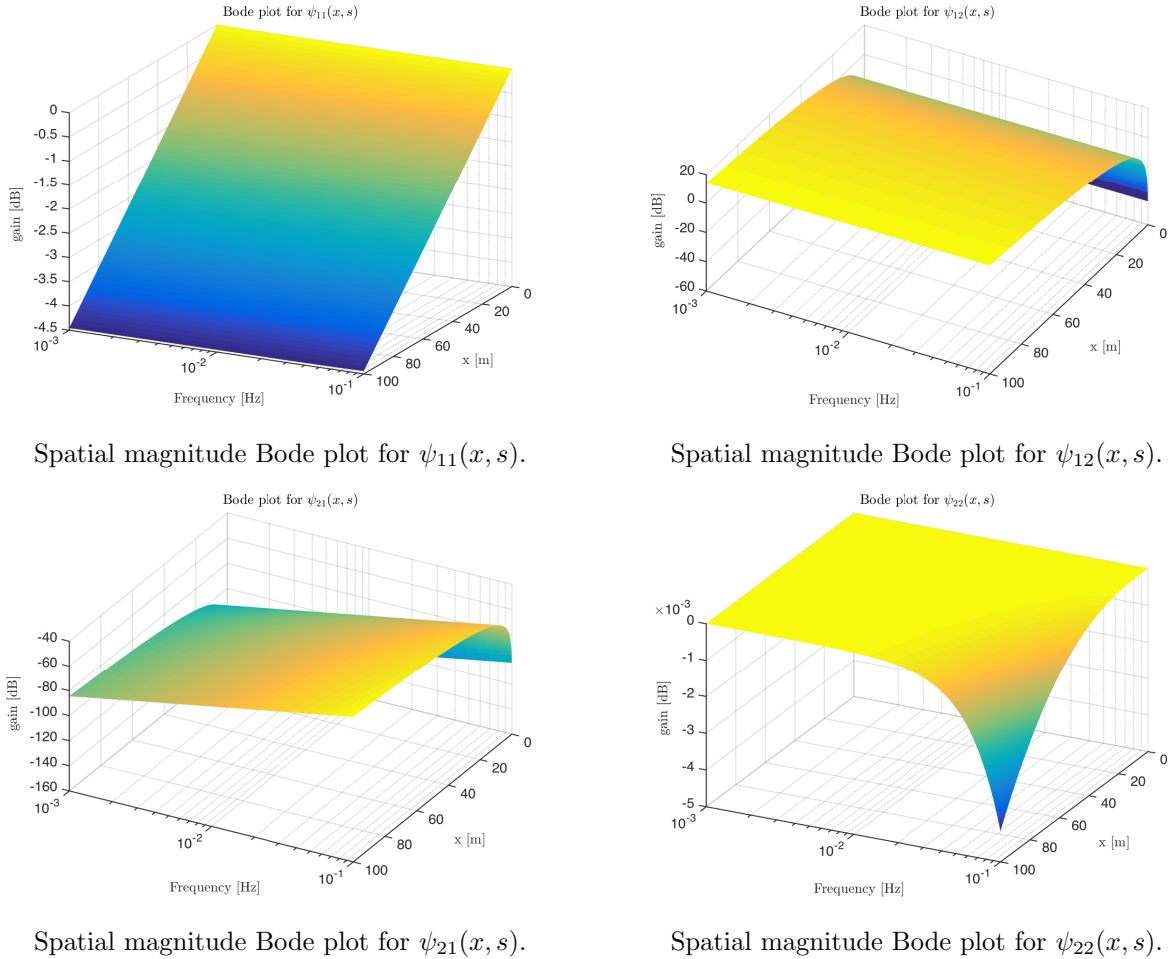


Figure 4: Spatial magnitude Bode plots for physical variables

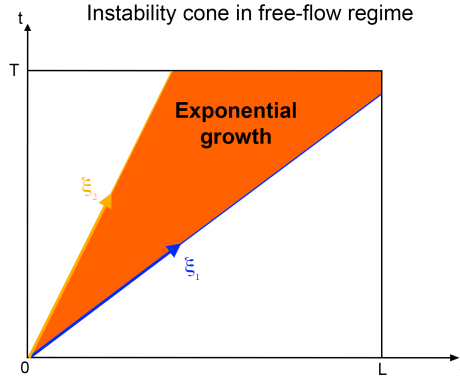


Figure 6: Illustration of the exponential growth cone appearing in the free-flowing regime for the time domain expressions of v and q .

With this set of time domain expressions, we can see that a cone of exponentially growing speed and flow generally appears between the characteristic lines corresponding to λ_1 and λ_2 . This is caused by α being negative in the free flow regime and means that, in this region of the domain $[0, T] \times [0, L]$, the (ρ, q) state of the linearized system can diverge exponentially fast from the linearization point.

3.3. Congested regime ($F > 1$)

We now consider the system in the congested regime.

Using (31) we can write

$$\begin{pmatrix} \hat{\xi}_1(x, s) \\ \hat{\xi}_2(x, s) \end{pmatrix} = \Phi(x, s) \underbrace{\begin{pmatrix} 1 & 0 \\ -\frac{\phi_{21}(L, s)}{\phi_{22}(L, s)} & \frac{1}{\phi_{22}(L, s)} \end{pmatrix}}_{\Gamma(x, s)} \begin{pmatrix} \hat{\xi}_1(0, s) \\ \hat{\xi}_2(L, s) \end{pmatrix}. \quad (42)$$

with

$$\gamma_{11}(x, s) = e^{-\frac{x}{\lambda_1}(s+\frac{1}{\tau})}, \quad (43a)$$

$$\gamma_{12}(x, s) = 0, \quad (43b)$$

$$\gamma_{21}(x, s) = \frac{\lambda_1}{\lambda_2} \frac{\alpha}{s + \alpha} e^{-\frac{s x}{\lambda_2}} e^{-\frac{x}{\lambda_1 \tau \alpha}(s+\alpha)} \left(1 - e^{-\frac{(L-x)}{\lambda_1 \tau \alpha}(s+\alpha)}\right), \quad (43c)$$

$$\gamma_{22}(x, s) = e^{-\frac{s(x-L)}{\lambda_2}}. \quad (43d)$$

Note that equation (42) corresponds to a closed form solution of our initial system, written in spectral form.

For low frequencies ($|s| \ll |\alpha|$), $\gamma_{21}(x, s) \simeq \frac{\lambda_1}{\lambda_2} e^{-\frac{s x}{\lambda_2}} e^{-\frac{x}{\lambda_1 \tau}} \left(1 - e^{-\frac{L-x}{\lambda_1 \tau}}\right)$ is the combination of a gain, a distributed delay with propagation speed $-\lambda_2$, and a distributed gain with characteristic distance $\lambda_1 \tau$ that cancels out for $x = L$. The resulting bode plot is presented below in Figure 7.

3.3.1. Transfer functions for physical variables in congested regime

In congested regime, the boundary conditions used to control the system are $\hat{x}_1(0, \cdot)$ and $\hat{x}_2(0, \cdot)$. By linearity of the Laplace transform $\hat{\xi}_1(\hat{0}, s) = \frac{\rho^* \lambda_2}{\lambda_1 - \lambda_2} \hat{v}(0, s) + \hat{q}(0, s)$. Therefore, as $\hat{\xi}_2(0, s) = \gamma_{21}(0, s) \hat{\xi}_1(0, s) + \gamma_{22}(0, s) \hat{\xi}_2(L, s)$, we get $\hat{\xi}_1(0, s) = \frac{1}{d(s)} \hat{q}(0, s) + \frac{n(s)}{d(s)} \hat{v}(L, s)$ where $d(s) = 1 - \frac{\lambda_2}{\lambda_1} \gamma_{21}(0, s)$ and $n(s) = \frac{\rho^* \lambda_2}{\lambda_1 - \lambda_2} \gamma_{22}(0, s)$. The (v, q) system has indeed only two degrees of freedom. Therefore we consider that the

only inputs to the system are $q(0, \cdot)$ and $v(L, \cdot)$. $v(0, \cdot)$ is then completely determined and can be interpreted as an output of the system. The corresponding transfer equation is

$$\begin{pmatrix} \hat{v}(x, s) \\ \hat{q}(x, s) \end{pmatrix} = Q^{-1} \Gamma(x, s) \underbrace{\begin{pmatrix} \frac{n(s)}{d(s)} & \frac{1}{d(s)} \\ \frac{\rho^* \lambda_1}{\lambda_1 - \lambda_2} & 0 \end{pmatrix}}_{\Theta(x, s)} \begin{pmatrix} \hat{v}(L, s) \\ \hat{q}(0, s) \end{pmatrix} \quad (44)$$

where

$$\theta_{11}(x, s) = \frac{\alpha e^{-\frac{x}{\tau \lambda_1}} e^{-\frac{s}{\lambda_1} (x - L \frac{\lambda_1}{\lambda_2})} + s e^{-\frac{s}{\lambda_2} (x - L)}}{s + \alpha e^{-\frac{x}{\tau \lambda_1}} e^{-\frac{s}{\lambda_1} (1 - \frac{\lambda_1}{\lambda_2})}}, \quad (45a)$$

$$\theta_{12}(x, s) = \frac{1}{\rho^* \tau} \frac{e^{-\frac{x}{\tau \lambda_1}} e^{-\frac{s}{\lambda_2} (x - L (1 - \frac{\lambda_2}{\lambda_1}))} - e^{-\frac{x}{\tau \lambda_1}} e^{-\frac{s x}{\lambda_1}}}{s + \alpha e^{-\frac{x}{\tau \lambda_1}} e^{-\frac{s}{\lambda_1} (1 - \frac{\lambda_1}{\lambda_2})}}, \quad (45b)$$

$$\theta_{21}(x, s) = \frac{\rho^* s}{\lambda_1 - \lambda_2} \frac{e^{-\frac{x}{\tau \lambda_1}} e^{-\frac{s}{\lambda_1} (x - L \frac{\lambda_1}{\lambda_2})} - e^{-\frac{s(x-L)}{\lambda_2}}}{s + \alpha e^{-\frac{x}{\tau \lambda_1}} e^{-\frac{s}{\lambda_1} (1 - \frac{\lambda_1}{\lambda_2})}}, \quad (45c)$$

$$\theta_{22}(x, s) = \frac{\alpha e^{-\frac{x}{\tau \lambda_1}} e^{-\frac{s}{\lambda_2} (x - L (1 - \frac{\lambda_2}{\lambda_1}))} + s e^{-\frac{x}{\tau \lambda_1}} e^{-\frac{s x}{\lambda_1}}}{s + \alpha e^{-\frac{x}{\tau \lambda_1}} e^{-\frac{s}{\lambda_1} (1 - \frac{\lambda_1}{\lambda_2})}}. \quad (45d)$$

3.3.2. Bode plots for congested regime

We use the same fundamental diagram as in the free-flow case. However the linearization point, $\rho^* = 0.08$ veh/m, corresponds to the congested region of the Greeshields diagram.

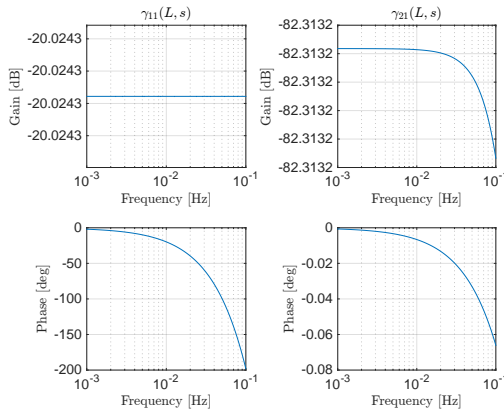
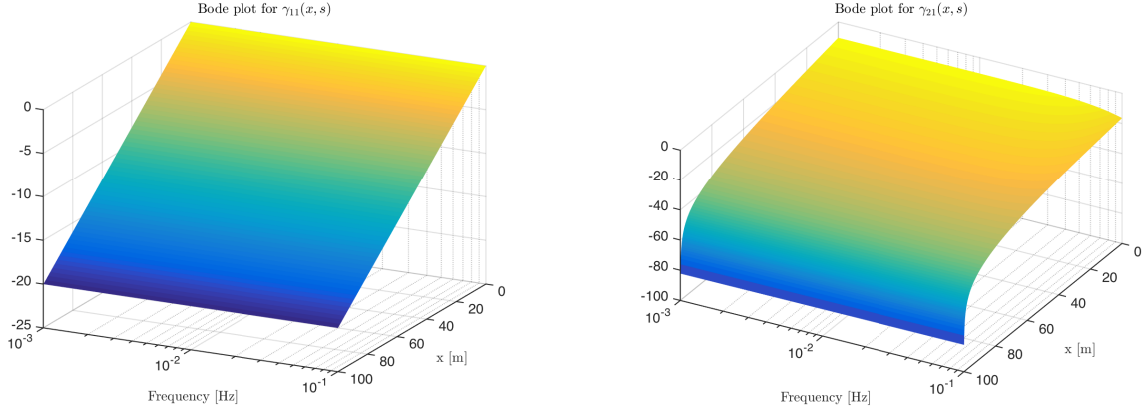


Figure 7: Magnitude and phase bode plots for $\gamma_{11}(L, s)$ and $\gamma_{21}(L, s)$ (left). (Riemann invariants).

3.4. Findings and conclusion from the theoretical study

The numerical experiments above have validated the accuracy of the linearized model and highlighted several of its core properties.

- The TFN delineates two regimes, congested, for $F > 1$ and free-flowing for $F < 1$. This classification, and the resulting stability result legitimize the use of linearization around a nominal point in the stable region.
- The assessment of instability in the free flow regime is of course applicable to this specific model (other models such as [18] might lead to other conclusions, and all need to be checked against experimental data). Here, instability only occurs in a conic region of the $[0, T] \times [0, L]$ domain.



Spatial magnitude Bode plot for $\gamma_{11}(x, s)$.

Spatial magnitude Bode plot for $\gamma_{21}(x, s)$.

Figure 8: Spatial magnitude Bode plots for Riemann invariants

- The absolute value of the term $\alpha = -\frac{\lambda_2}{\tau(\lambda_1 - \lambda_2)}$ is a characteristic frequency for the system. It delineates the low frequency domain in which approximate expressions help decompose the transfer functions in gain and delay components. In the spectral domain, λ_1 and λ_2 do appear as information propagation speed. In several gain elements, $\tau\lambda_1$ and $\tau\lambda_2$ act as characteristic damping distances.

4. Numerical validation

In this section we demonstrate the ability of the linearized ARZ equations to model the various nonlinear dynamics around a nominal operation point. The spectral form of the linearized model provides a well-established control theoretic framework for designing control strategies for the system. Prior to using such techniques, it is necessary to assess how accurate the model is in its linearized form. This section compares the prediction of the model with actual flow and velocity data gathered from the well-known NGSIM data set.

4.1. Data source: NGSIM trajectories

We use the NGSIM trajectory data set for a section of the US-101 highway. The set gathers trajectories of vehicles sampled with a 10 Hz frequency thanks to high precision cameras. The data is pre-processed so as to take only cars into account; 45 minutes are recorded on a 650-meter long section with five lanes. The lanes are taken into account when computing the lineic density of vehicles ρ . A map of the time evolution of speed along the section is given in Figure 9. Only a subset of the spatial domain is used due to the presence of ramps, which breaks the homogeneity of the freeway. The viable domain is 200 meters long.

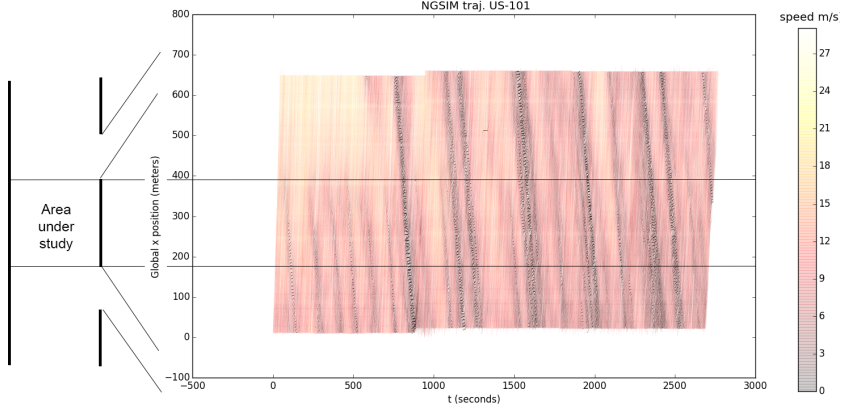


Figure 9: NGSIM trajectories. Color represents the measured speed of each car in m/s.

4.2. Reconstructing (v, q) maps from NGSIM trajectories

The NGSIM data set does not directly provide the values $v(t, x)$ and $q(t, x)$ in the resolution domain $[0, T] \times [0, L]$. To obtain macroscopic quantities out of the microscopic measurements, we follow the approach devised in [41] and divide the space-time grid into cells $([i\Delta t, (i+1)\Delta t] \times [j\Delta x, (j+1)\Delta x])_{i \in \{1 \dots n_t\}, j \in \{1 \dots n_x\}}$, where n_t and n_x are the number of cells in time and space, respectively. We denote each cell as $\text{bin}_{i,j}$. This operation consists of gathering corresponding data points into cells, then estimating the quantities of interest in each cell.

Within each cell, a specific number of traces, or footprints of a vehicle along its trajectory, are available, and ρ , v , and q are assumed to be constant. We present several formulae to map a set of traces to speed, flow, and density over the space-time grid.

Binning formula for v : Since the speed is assumed to be constant in each cell, a straightforward estimate for the speed is the empirical average. The estimator for v in $\text{bin}_{i,j}$ is

$$\hat{v}_{i,j} = \text{mean}_{\text{trace} \in \text{bin}_{i,j}}(v(\text{trace})). \quad (46)$$

Binning formula for ρ : By definition, the density of $\text{bin}_{i,j}$ is

$$\rho_{i,j} = \frac{1}{n_{\text{lanes}} \Delta x \Delta t} \iint_{(t,x) \in [i\Delta t, (i+1)\Delta t] \times [j\Delta x, (j+1)\Delta x]} \rho(x, t) dx dt. \quad (47)$$

The position of each vehicle is recorded every 0.1 second. For each cell we count the number of traces and normalize it by the sampling rate. The contribution of a given vehicle to the density of a cell is proportional to the number of traces it has left in the cell. If the speed is assumed to be locally constant, this contribution is proportional to the time this vehicle spends in the cell and is consistent with the conservation of the total number of vehicles across all cells. Then we have the density estimator

$$\hat{\rho}_{i,j} = \frac{1}{n_{\text{lanes}} \Delta x \Delta t \text{ sampling rate}} \text{card}(\{\text{trace} \mid \text{trace} \in \text{bin}\}), \quad (48)$$

where $\text{card}(\cdot)$ gives the number of elements in a set, i.e., its cardinal.

Binning formula for q : By definition, $q = \rho v$, so a logical first estimate for q in $\text{bin}_{i,j}$ is

$$\hat{q}_{i,j} = \hat{v}_{i,j} \hat{\rho}_{i,j}. \quad (49)$$

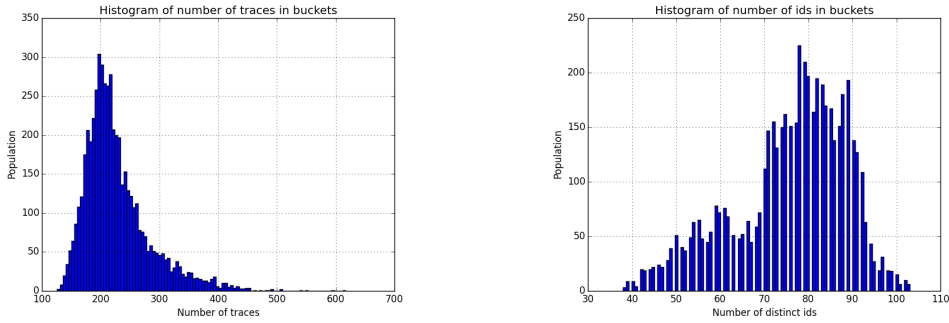
We can also approximate the flux through $\text{bin}_{i,j}$ with a simple counting method. If a vehicle crosses spatial coordinate $(j+1)\Delta x$ between times $i\Delta t$ and $(i+1)\Delta t$, then it leaves a trace in both $\text{bin}_{i,j}$ and $\text{bin}_{i,j+1}$. Counting these vehicles and normalizing by the duration Δt gives the estimator

$$\hat{q}_{i,j}^{\text{count}} = \frac{1}{n_{\text{lanes}} \Delta t} \text{card}(\{\text{id}(\text{trace}) \mid \text{trace} \in \text{bin}_{i,j} \cap \{\text{id}(\text{trace}) \mid \text{trace} \in \text{bin}_{i,j+1}\}\}), \quad (50)$$

where $\text{id}(\cdot)$ gives the identification number of a vehicle.

4.2.1. Choosing the number of bins

As the estimation formulae above rely on averaging, having a comfortable number of points in each bin provides more stable estimates. It is worth mentioning that usual central limit theorem based reasoning for convergence of such estimates is flawed as several samples may correspond to the same vehicle or interacting vehicles, violating the independence assumption of the theorem. Proving the convergence of the estimates above lies beyond the scope of this article. As a rule of thumb we choose a discretization that guarantees that most bins will host more than 100 traces. This is achieved with a 80×80 grid where the 10th percentile of the number of traces in a given bin is 170. Such a grid also yields a 10th percentile of 56 distinct vehicles per bin. The histograms of number of traces and vehicle per cell are given in Figure 10.



Histogram of number of traces per cell. Histogram of number of distinct vehicles per cell.

Figure 10: Experimental justification for a 80×80 cell based discretization grid for the NGSIM data.

While our goal here is not to present theoretical proofs of the convergence of the binned estimators for (v, ρ, q) , it is nonetheless possible to check that the procedure is coherent. Two estimators are provided for q that use radically different techniques: the first relies on the average measured speed and the number of traces in a bin, while the other relies on counting vehicles transiting from a cell to another. Figure 11 show that the scatter plot of $\hat{q}_{i,j}^{\text{count}}$ plotted against $\hat{q}_{i,j}$ coincides nicely with the line $y = x$, validating the overall binning and estimation procedure above.

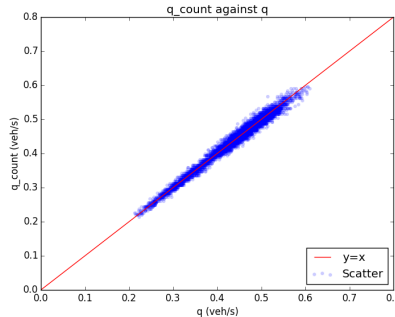


Figure 11: Sanity check for the estimation procedure. $\hat{q}_{i,j}^{\text{count}}$ is plotted against $\hat{q}_{i,j}$ across the grid of bins.

4.3. Estimated values for (v, q)

To check how well the linearized ARZ model fits an actual dataset, we chose a bounded domain and compare the theoretical solution given by the second-order model and the observed data. Again we focus on the variables v and q . Using the estimation procedure above, we compute fundamental diagrams from which we estimate the eigenvalues λ_1 and λ_2 . To calibrate the relaxation time τ , we analyze the errors of predicted values of v and q for various τ . The resulting maps of both the predicted and observed values highlight phenomena that the linearized model can and cannot account for.

Maps. The estimates $\hat{v}_{i,j}$, $\hat{\rho}_{i,j}$, $\hat{q}_{i,j}$, and $\hat{q}_{i,j}^{\text{count}}$ are plotted on the discretized grid in Figure 12. Note that \hat{q} and \hat{q}^{count} give extremely similar results, so we may use \hat{q}^{count} from this point on. Damped oscillations and

smoothly decaying values along characteristic lines are the main characteristic the practical implementation of the model should feature.

Fundamental diagrams. From the estimated values we can easily compute the fundamental diagrams given in Figure 13. We use the fundamental diagrams to calibrate the model parameters. Though the dataset used is dense, it covers only a small region of time and space. Thus, its small size is a potential flaw in our model parameter calibration as it is certain that our measurements are highly correlated. This seems to be confirmed by the fact that the fundamental diagrams below correspond only to the congested regime.

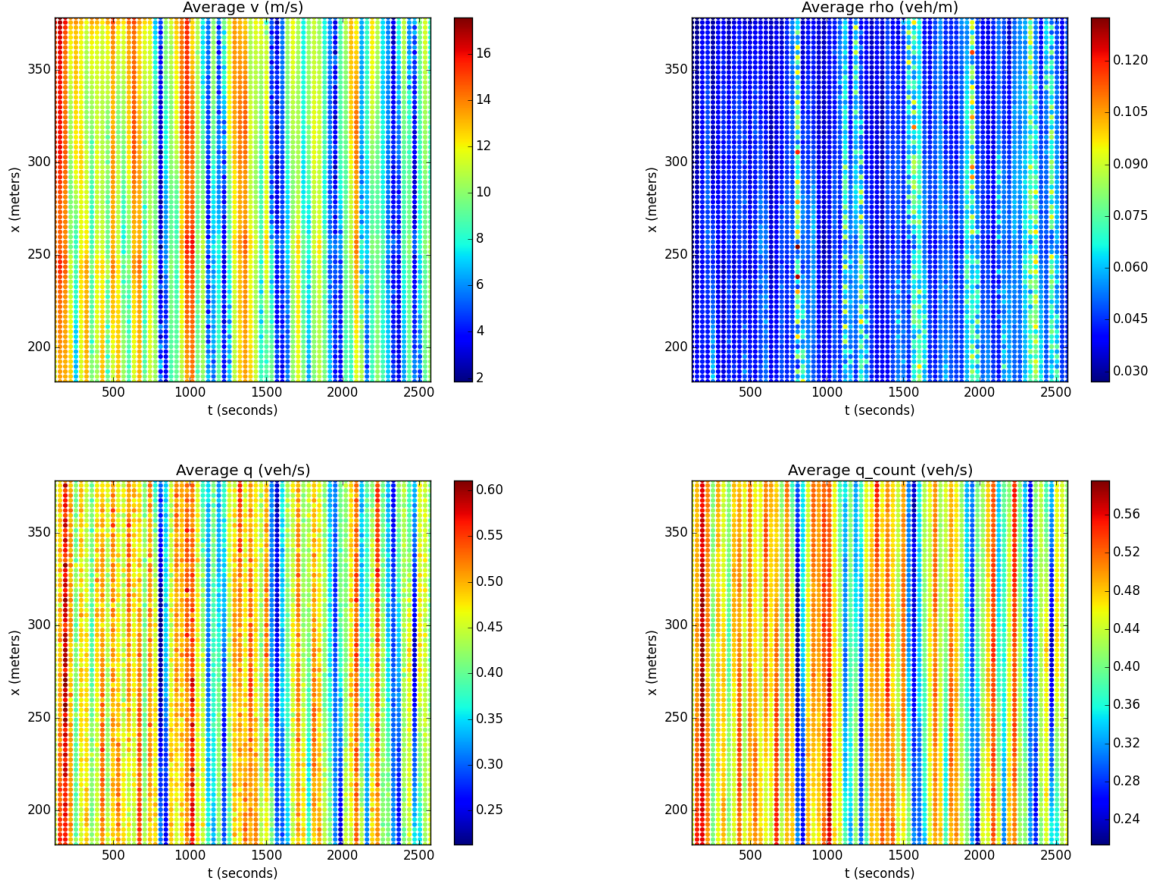


Figure 12: Estimated values for (v, q, ρ) . Top left: $\hat{v}_{i,j}$. Top right: $\hat{\rho}_{i,j}$. Bottom left: $\hat{q}_{i,j}$. Bottom right: $\hat{q}_{i,j}^{\text{count}}$.

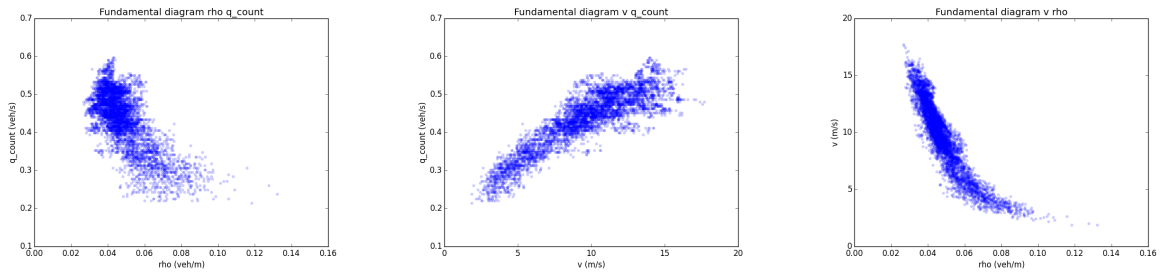


Figure 13: Empirical fundamental diagrams. Left: $(\hat{\rho}, \hat{q}^{\text{count}})$. Middle: $(\hat{v}, \hat{q}^{\text{count}})$. Right: $(\hat{\rho}, \hat{v})$.

Calibration of λ_1 and λ_2 , linearization point. In Section 2, we found that λ_1 is exactly v^* and λ_2 is

the slope of the fundamental diagram at v^* . Thus to calibrate the eigenvalues we must find the linearization point. We estimate the linearization point using the Ordinary Least Squares method. Note the dataset used corresponds only to the congested regime and the fundamental diagram is almost affine. The estimator, $\hat{\lambda}_1 = \hat{v}^*$ is chosen as the empirical mean of $\hat{v}_{i,j}$. To estimate λ_2 , we fit a linear model $\hat{q}^{\text{count}} = b_1\hat{\rho} + b_0 + \varepsilon$, where ε represents the noise in the model that would ideally be centered, homoschedastic, and uncorrelated but is not practically. Then $\hat{\lambda}_2 = \hat{b}_1$ and we take \hat{q}^* as the empirical average of \hat{q}^{count} . The ratio of \hat{q}^* and \hat{v}^* gives the estimate $\hat{\rho}^*$. Provided each estimator is convergent, the continuity of the functional $(x, y) \rightarrow \frac{x}{y}$ on its domain guarantees the convergence of $\hat{\rho}^*$. The empirical results are presented in Figure 14. The determination coefficient is poor but can be improved by filtering out outliers and gathering more data. Future work should include improving the quality of the estimation. Significance tests for the coefficients of the linear model are not presented. The assumptions they rely on about the linear dependency between \hat{q} and \hat{v} are clearly not respected here as the noise is auto-correlated. Further work should also to turn this rather heuristic method for estimating parameters into a fully justified statistical procedure. Note that the goal of the present article is to provide a new model and corresponding spectral analysis, which we want to illustrate with state of the art data. Thus, development of statistical methods to handle this data is out of the scope of the present investigation.

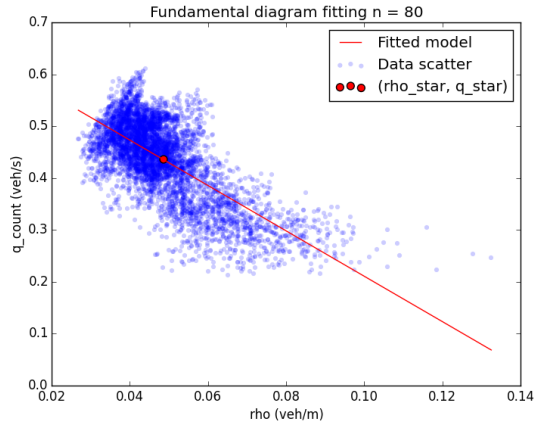


Figure 14: Calibration of λ_1 and λ_2 . The circle denotes the linearization point. The affine model used to estimate λ_2 and the linearization point is also plotted. The estimates are: $\hat{\lambda}_1 = 8.96$ m/s, $\hat{\lambda}_2 = -4.37$ m/s, $\hat{\rho}^* = 0.049$ veh/m, $\hat{v}^* = 8.96$ m/s, $\hat{q}^* = 0.44$ veh/s, with $r^2 = 0.48$

4.4. Verification of the spectral form

In this section we demonstrate the performance of the spectral form as a prediction tool using the time domain responses derived from the transfer functions (see Appendix A) and FFT. Since we are working with a linearized system, we can decompose boundary conditions then add predicted values inside the domain $[0, T] \times [0, L]$. Fourier decomposition of boundary conditions is here extremely accurate as the median relative errors for the interpolation of the values of $\xi_1(x = 0, \cdot)$ and $\xi_2(x = L, \cdot)$ are respectively 2% and 3%.

Simulated maps. Since the spectral form presents information in the diagonalized basis, we need a conversion before we can compare the simulated results to the values estimated from the dataset. To make a comparison in the diagonalized basis, we first compute the estimated deviations from the equilibrium $\hat{\tilde{v}}_{i,j} = \hat{v}_{i,j} - \hat{v}^*$ and $\hat{\tilde{q}}_{i,j} = \hat{q}_{i,j} - \hat{q}^*$. Then the estimates for ξ_1 and ξ_2 are given by $\hat{\xi}_{1,i,j} = \frac{\hat{\rho}^* \hat{\lambda}_2}{\hat{\lambda}_1 - \hat{\lambda}_2} \hat{\tilde{v}}_{i,j} + \hat{\tilde{q}}_{i,j}$ and $\hat{\xi}_{2,i,j} = \frac{\hat{\rho}^* \hat{\lambda}_1}{\hat{\lambda}_1 - \hat{\lambda}_2} \hat{\tilde{v}}_{i,j}$. To compare the physical variables, we compute the velocity and flow predictions by inverting (27): $\tilde{q} = \xi_1 - \frac{\lambda_1}{\lambda_2} \xi_2$, $\tilde{v} = \frac{\lambda_1 - \lambda_2}{\rho^* \lambda_1} \xi_2$.

Figure 15 shows important qualitative properties of the model. As expected, the model generally predicts with very good accuracy the decay of all quantities along their characteristic lines, a realistic feature that cannot be paralleled by first-order models. The general quality of the fit is rather good with most of the error on v and q in a 20% range of the data's amplitude between minimum and maximum values. Furthermore

the linearized second-order model manages to capture oscillations observed on the boundary and account for their decay accurately.

Calibration of τ For each τ we compute the *mean absolute error* (MAE), or the average difference in absolute value between simulated and predicted values for each discretization cell. Since the quantities v and q are not physically homogeneous, it is not sensible to aggregate the errors over these quantities. However, ξ_1 and ξ_2 are both expressed in veh/s. Summing their MAE gives a reliable uni-dimensional index of the quality of the fit with respect to τ . This quantity is computed for different values of τ ranging from 5 to 80 seconds. The value offering the best fit is $\tau^* = 39.18$ s.

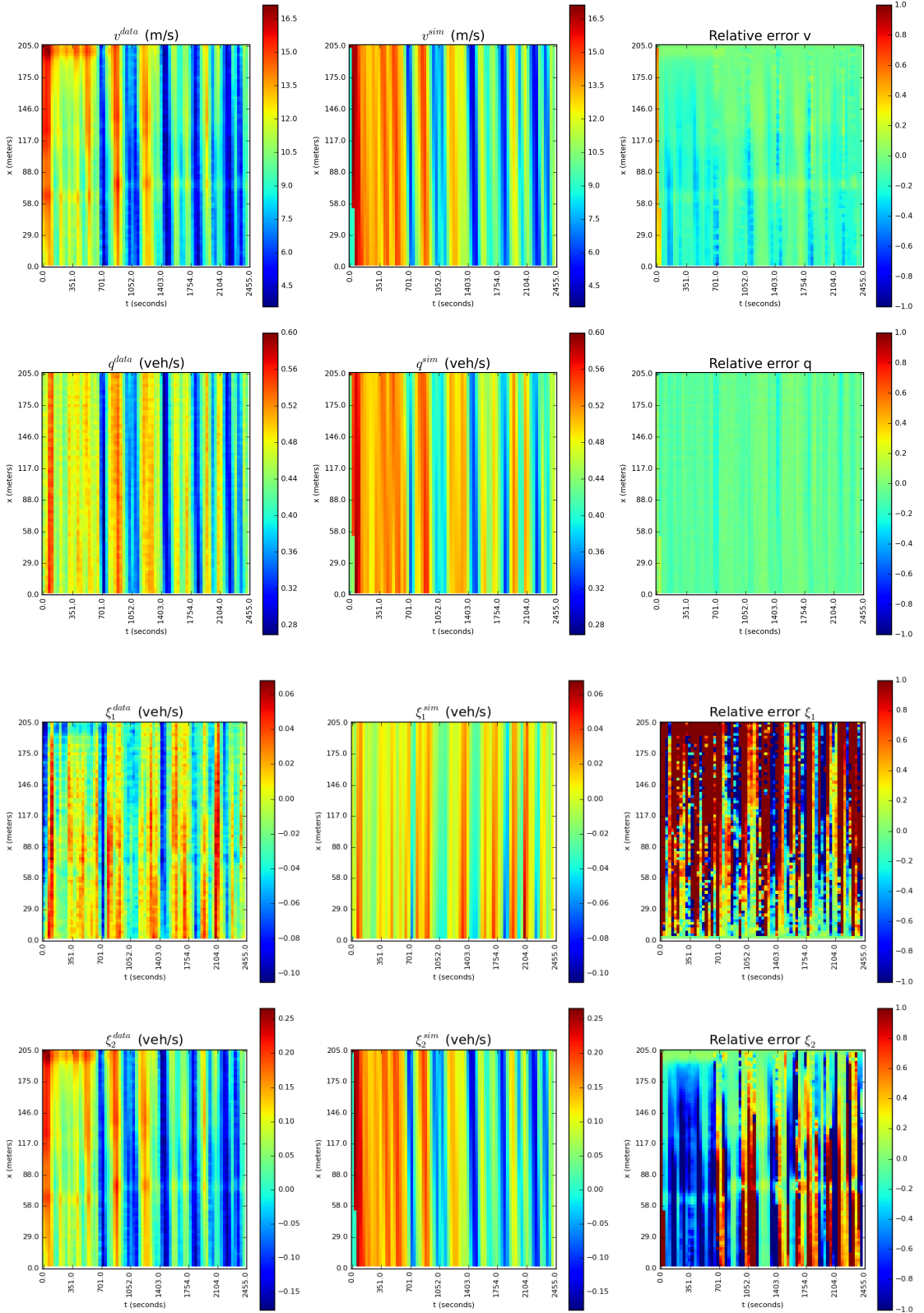


Figure 15: Data versus predicted. Top Figure: (v, q) domain, top row is v , bottom row is q . Bottom: (ξ_1, ξ_2) domain, top row is ξ_1 , bottom row is ξ_2 . First column: data. Middle column: predictions. Third column: error (difference between prediction and data).



Figure 16: Calibration of τ , one minimizes the sum of MAE over ξ_1 and ξ_2 .

4.5. Findings and conclusion from the numerical experiments

The numerical experiments above have validated the accuracy of the linearized model and highlighted several of its core properties.

- The numerical experiments above show that the linearized ARZ model is capable of reproducing NGSIM data accurately for a homogeneous segment of the US-101 freeway. Oscillations are accounted for as well as their damping delay.
- The spectral approach provided here supports a solution to the underlying traffic flow model. In other words, the contribution of the work is to show that the model can support oscillatory behavior (through periodic solutions). This is the main difference with purely data driven approaches such as [36] for example.

5. Conclusion

As the full nonlinear ARZ equations have no known closed form solutions in the general case, they are difficult to analyze. The linearized equations enable the use of spectral methods presented here, allowing for elegantly simple yet powerful analysis tools relying on explicit solutions. These equations are diagonalized, and solved explicitly using a spectral representation (distributed transfer function). Using this approximation, we are able to analyze them around a nominal flow and characterize the oscillatory behavior of the solution. The linearized model is able to capture important features of the flow which first order models cannot.

With the linearized ARZ model, we were also able to define the Traffic Froude Number F . This quantity is computed using the eigenvalues of the system and characterizes the flow regime of the road section under consideration.

Considering the transfer function of the linearized system of equations delineates the conditions for stability of the approximation about the equilibrium. The time domain responses we derive show that the system is unstable when one of the eigenvalues is negative. In the free-flow regime, $F < 1$, values of flow and speed increase exponentially in a conic region of space and time and the system leaves the linear regime, while in the congested regime, $F > 1$, oscillations decrease. In the latter case, the system remains in the linear regime and oscillations on boundary conditions are damped with an exponential rate along the characteristic lines. Thus, the TFN is also an indicator of linear stability.

The behavior predicted in congested regime for traffic does not present shocks and Fourier spectral analysis cannot account for more nonlinear and non-smooth behavior as well as wavelet transforms. However, our spectral domain study paves the way to applying standard linear system control theory to traffic, with a linearized second model that is empirically reliable in terms of reproducing actual data. Future work will therefore focus on controller design based on the spectral framework presented here.

Appendix A. Generic computations for time domain to Laplace domain transforms and vice versa

The aim is to derive the time domain responses of generic input signals such as $t \rightarrow H(t)$ and $t \rightarrow \cos(wt + \phi) H(t)$ when multiplied in the Laplace domain by $\frac{1}{s+\alpha}$. This then enables the computation of any response that decomposes in a Fourier transform.

Appendix A.1. Step function input

The time domain input function is $H(t)$. One computes the inverse Laplace transform of $s \rightarrow \frac{1}{s(s+\alpha)}$ which is

$$t \rightarrow \frac{1}{\alpha} (1 - e^{-\alpha t}) H(t)$$

Appendix A.2. Phased cosine input

The time domain input function is $\cos(wt + \phi) H(t)$. One computes the inverse Laplace transform of $s \rightarrow \frac{1}{s+\alpha} \left\{ \frac{s}{s^2 + \omega^2} \cos(\phi) - \frac{w}{s^2 + \omega^2} \sin(\phi) \right\}$ which can be directly achieved in the time domain. Indeed, the result is given by the convolution product $t \rightarrow (e^{-\alpha t} H(\cdot) \star \cos(\omega \cdot + \phi) H(\cdot))(t)$, that is to say

$$t \rightarrow \frac{-e^{-\alpha \cdot t} (\alpha \cdot \cos(\phi) + w \cdot \sin(\phi)) + \alpha \cdot \cos(wt + \phi) + w \cdot \sin(wt + \phi)}{\alpha^2 + w^2} H(t) = \kappa_{\alpha, w, \phi}^{\cos}(t)$$

Appendix A.3. Fourier sum input

Let the input be $t \rightarrow \mu H(t) + \sum_{k=1}^n \beta_k \cdot \cos(k \cdot wt + \phi_k) H(t)$. The time domain response is therefore

$$t \rightarrow \frac{\mu}{\alpha} (1 - e^{-\alpha t}) H(t) + \sum_{k=1}^n \beta_k \cdot \kappa_{\alpha, w, \phi}^{\cos}(t)$$

Appendix A.4. Fourier decomposition and time domain responses for $\lambda_2 > 0$

Let $\alpha = -\frac{\lambda_2}{\tau(\lambda_1 - \lambda_2)} < 0$.

$$\begin{pmatrix} \widehat{\xi}_1(x, s) \\ \widehat{\xi}_2(x, s) \end{pmatrix} = \Phi(x, s) \begin{pmatrix} \widehat{\xi}_1(0, s) \\ \widehat{\xi}_2(0, s) \end{pmatrix}$$

with

$$\Phi(x, s) = \begin{bmatrix} e^{-\frac{sx}{\lambda_1}} e^{-\frac{x}{\lambda_1 \tau}} & 0 \\ -\alpha \frac{\lambda_1}{\lambda_2} \left(e^{-\frac{sx}{\lambda_1}} e^{-\frac{x}{\lambda_1 \tau}} - e^{-\frac{sx}{\lambda_2}} \right) \frac{1}{s+\alpha} & e^{-\frac{sx}{\lambda_2}} \end{bmatrix}$$

implies the following fundamental responses for the system.

Appendix A.4.1. Fundamental responses in time domain:

- $\begin{pmatrix} \xi_1(0, t) \\ \xi_2(0, t) \end{pmatrix} = \begin{pmatrix} H(t) \\ 0 \end{pmatrix}$:

- $\xi_1(x, t) = e^{-\frac{x}{\lambda_1 \tau}} H\left(t - \frac{x}{\lambda_1}\right)$
- $\xi_2(x, t) = -\frac{\lambda_1}{\lambda_2} \left(e^{-\frac{x}{\lambda_1 \tau}} \left(1 - e^{-\alpha(t - \frac{x}{\lambda_1})} \right) H\left(t - \frac{x}{\lambda_1}\right) - \left(1 - e^{-\alpha(t - \frac{x}{\lambda_2})} \right) H\left(t - \frac{x}{\lambda_2}\right) \right)$

- $\begin{pmatrix} \xi_1(0, t) \\ \xi_2(0, t) \end{pmatrix} = \begin{pmatrix} 0 \\ H(t) \end{pmatrix}$:

- $\xi_1(x, t) = 0$

- $\xi_2(x, t) = H\left(t - \frac{x}{\lambda_2}\right)$

- $\begin{pmatrix} \xi_1(0,t) \\ \xi_2(0,t) \end{pmatrix} = \begin{pmatrix} \cos(\omega t + \phi) \\ 0 \end{pmatrix}$:
 - $-\xi_1(x,t) = e^{-\frac{x}{\lambda_1\tau}} \cos\left(\omega\left(t - \frac{x}{\lambda_1}\right) + \phi\right) H\left(t - \frac{x}{\lambda_1}\right)$
 - $-\xi_2(x,t) = -\frac{\lambda_1\alpha}{\lambda_2} \left(e^{-\frac{x}{\lambda_1\tau}} \kappa_{\alpha,\omega,\phi}^{\cos}\left(t - \frac{x}{\lambda_1}\right) - \kappa_{\alpha,\omega,\phi}^{\cos}\left(t - \frac{x}{\lambda_2}\right)\right)$
- $\begin{pmatrix} \xi_1(0,t) \\ \xi_2(0,t) \end{pmatrix} = \begin{pmatrix} 0 \\ \cos(\omega t + \phi) \end{pmatrix}$:
 - $-\xi_1(x,t) = 0$
 - $-\xi_2(x,t) = \cos\left(\omega\left(t - \frac{x}{\lambda_2}\right) + \phi\right) H\left(t - \frac{x}{\lambda_2}\right)$

Appendix A.5. Fourier decomposition and time domain responses for $\lambda_2 < 0$

This time, $\alpha = -\frac{\lambda_2}{\tau(\lambda_1 - \lambda_2)} > 0$.

$$\begin{pmatrix} \widehat{\xi}_1(x,s) \\ \widehat{\xi}_2(x,s) \end{pmatrix} = \Phi(x,s) \begin{pmatrix} \widehat{\xi}_1(0,s) \\ \widehat{\xi}_2(L,s) \end{pmatrix}$$

with

$$\Gamma(x,s) = \begin{pmatrix} e^{-\frac{sx}{\lambda_1}} e^{-\frac{x}{\lambda_1\tau}} & 0 \\ \alpha \frac{\lambda_1}{\lambda_2} \left(e^{-\frac{x}{\lambda_1\tau}} e^{-\frac{sx}{\lambda_1}} - e^{-\frac{L}{\lambda_1\tau}} e^{-\frac{s}{\lambda_2}(x-L\frac{\lambda_1-\lambda_2}{\lambda_1})}\right) \frac{1}{s+\alpha} & e^{-\frac{s(x-L)}{\lambda_2}} \end{pmatrix}$$

implies the following fundamental responses for the system.

Appendix A.5.1. Fundamental responses in time domain

- $\begin{pmatrix} \xi_1(0,t) \\ \xi_2(L,t) \end{pmatrix} = \begin{pmatrix} H(t) \\ 0 \end{pmatrix}$:
 - $-\xi_1(x,t) = e^{-\frac{x}{\lambda_1\tau}} H\left(t - \frac{x}{\lambda_1}\right)$
 - $-\xi_2(x,t) = \frac{\lambda_1}{\lambda_2} \left(e^{-\frac{x}{\lambda_1\tau}} \left(1 - e^{-\alpha\left(t - \frac{x}{\lambda_1}\right)}\right) H\left(t - \frac{x}{\lambda_1}\right) - e^{-\frac{L}{\lambda_1\tau}} \left(1 - e^{-\alpha\left(t - \frac{x-L\frac{\lambda_1-\lambda_2}{\lambda_1}}{\lambda_2}\right)}\right) H\left(t - \frac{x-L\frac{\lambda_1-\lambda_2}{\lambda_1}}{\lambda_2}\right)\right)$
- $\begin{pmatrix} \xi_1(0,t) \\ \xi_2(L,t) \end{pmatrix} = \begin{pmatrix} 0 \\ H(t) \end{pmatrix}$:
 - $-\xi_1(x,t) = 0$
 - $-\xi_2(x,t) = H\left(t - \frac{x-L}{\lambda_2}\right)$
- $\begin{pmatrix} \xi_1(0,t) \\ \xi_2(L,t) \end{pmatrix} = \begin{pmatrix} \cos(\omega t + \phi) \\ 0 \end{pmatrix}$:
 - $-\xi_1(x,t) = e^{-\frac{x}{\lambda_1\tau}} \cos\left(\omega\left(t - \frac{x}{\lambda_1}\right) + \phi\right) H\left(t - \frac{x}{\lambda_1}\right)$
 - $-\xi_2(x,t) = \frac{\lambda_1\alpha}{\lambda_2} \left(e^{-\frac{x}{\lambda_1\tau}} \kappa_{\alpha,\omega,\phi}^{\cos}\left(t - \frac{x}{\lambda_1}\right) - e^{-\frac{L}{\lambda_1\tau}} \kappa_{\alpha,\omega,\phi}^{\cos}\left(t - \frac{x-L\frac{\lambda_1-\lambda_2}{\lambda_1}}{\lambda_2}\right)\right)$
- $\begin{pmatrix} \xi_1(0,t) \\ \xi_2(L,t) \end{pmatrix} = \begin{pmatrix} 0 \\ \cos(\omega t + \phi) \end{pmatrix}$:
 - $-\xi_1(x,t) = 0$
 - $-\xi_2(x,t) = \cos\left(\omega\left(t - \frac{x-L}{\lambda_2}\right) + \phi\right) H\left(t - \frac{x-L}{\lambda_2}\right)$

Acknowledgments

References

- [1] M. J. Lighthill, J. B. Whitham, On kinematic waves. II: A theory of traffic flow on long crowded roads, *Proc. Royal. Soc.* (1955) 317–345.
- [2] P. I. Richards, Shock waves on the highway, *Operations Research* 4 (1) (1956) 42–51.
- [3] B. D. Greenshields, A study of traffic capacity, in: *Highway Research Board Proceedings*, 1934, pp. 448–474.
- [4] H. Greenberg, An analysis of traffic flow, *Operations Research* 7 (1) (1959) 79–85.
- [5] G. F. Newell, A simplified theory of kinematic waves in highway traffic, part II: queueing at freeway bottlenecks, *Transp. Res. Part B* 27 (7) (1993) 289–303.
- [6] C. F. Daganzo, The cell transmission model: A dynamic representation of highway traffic consistent with the hydrodynamic theory, *Transp. Res. Part B* 28 (4) (1994) 269–287.
- [7] Y. Wang, M. Papageorgiou, Real-time freeway traffic state estimation based on extended Kalman filter: a general approach, *Transportation Research Part B: Methodological* 39 (2) (2005) 141 – 167.
- [8] Macroscopic modelling of traffic flow on the Boulevard Peripherique in Paris, *Transportation Research Part B: Methodological* 23 (1) (1989) 29 – 47.
- [9] M. R. Flynn, A. R. Kasimov, J. c. Nave, R. R. Rosales, B. Seibold, Self-sustained nonlinear waves in traffic flow, *Physical Review E* 79 (2009) 56–113.
- [10] M. Treiber, A. Kesting, Traffic flow dynamics, *Traffic Flow Dynamics: Data, Models and Simulation*, ISBN 978-3-642-32459-8. Springer-Verlag Berlin Heidelberg, 2013 1.
- [11] M. Garavello, B. Piccoli, *Traffic Flow on Networks: Conservation Laws Models*, AIMS series on applied mathematics, American Institute of Mathematical Sciences, 2006.
- [12] S. K. Godunov, A difference scheme for numerical solution of discontinuous solution of hydrodynamic equations, *Math. Sbornik* 47 (1969) 271–306.
- [13] S. Osher, Riemann solvers, the entropy condition, and difference, *SIAM Journal on Numerical Analysis* 21 (2) (1984) 217–235.
- [14] C. F. Daganzo, The cell transmission model, part II: network traffic, *Transp. Res. Part B* 29 (2) (1995) 79–93.
- [15] C. F. Daganzo, Requiem for second-order fluid approximations of traffic flow, *Transp. Res. Part B* 29 (4) (1995) 277–286.
- [16] Y. Sugiyama, M. Fukui, M. Kikuchi, K. Hasebe, A. Nakayama, K. Nishinari, S. ichi Tadaki, S. Yukawa, Traffic jams without bottlenecks, experimental evidence for the physical mechanism of the formation of a jam, *New J. Phys.*
- [17] M. R. Flynn, A. R. Kasimov, J. c. Nave, R. R. Rosales, B. Seibold, On jamitons, self-sustained nonlinear traffic waves (2008).
- [18] B. Seibold, M. R. Flynn, A. R. Kasimov, R. R. Rosales, Constructing set-valued fundamental diagrams from jamiton solutions in second order traffic models, ArXiv e-prints [arXiv:1204.5510](https://arxiv.org/abs/1204.5510).
- [19] H. J. Payne, *Models of Freeway Traffic and Control*, Simulation Councils, Incorporated, 1971.
- [20] G. B. Whitham, *Linear and Nonlinear Waves*, A Wiley-Interscience publication, Wiley, 1974.

- [21] G. F. Newell, Nonlinear effects in the dynamics of car following, *Operations Research* 9 (2) (1961) 209–229.
- [22] H. M. Zhang, A non-equilibrium traffic model devoid of gas-like behavior, *Transp. Res. Part B* 36 (2002) 275–290.
- [23] H. M. Zhang, A theory of nonequilibrium traffic flow, *Transp. Res. Part B* 32 (7) (1998) 485–498.
- [24] A. Aw, M. Rascle, Resurrection of second order models of traffic flow, *SIAM Journal of Applied Mathematics* 60 (3) (2000) 916–938.
- [25] M. Rascle, An improved macroscopic model of traffic flow: derivation and links with the Lighthill-Whitham model, *Mathematical and computer modelling* 35 (2002) 581–590.
- [26] J.-P. Lebacque, S. Mammar, H. Haj-Salem, The aw–rascle and zhang’s model: Vacuum problems, existence and regularity of the solutions of the riemann problem, *Transp. Res. Part B* 41 (7) (2007) 710–721.
- [27] S. Moutari, M. Rascle, A hybrid lagrangian model based on the Aw–Rascle traffic flow model, *SIAM Journal on Applied Mathematics* 68 (2) (2007) 413–436.
- [28] M. Garavello, B. Piccoli, Traffic flow on a road network using the Aw–Rascle model, *Communications in Partial Differential Equations* 31 (2) (2006) 243–275.
- [29] S. Mammar, J.-P. Lebacque, H. H. Salem, Riemann problem resolution and godunov scheme for the aw–rascle–zhang model, *Transportation Science* 43 (4) (2009) 531–545.
- [30] S. Fan, M. Herty, B. Seibold, Comparative model accuracy of a data-fitted generalized aw–rascle–zhang model, *Networks and Heterogeneous Media* 9 (2) (2014) 239–268.
- [31] J. M. Greenberg, Congestion redux, *SIAM J. Appl. Math* 64 (2004) 1175–1185.
- [32] D. Chen, J. Laval, Z. Zheng, S. Ahn, A behavioral car-following model that captures traffic oscillations, *Transp. Res. Part B* 46 (6) (2012) 744–761.
- [33] M. Mauch, M. J. Cassidy, Freeway traffic oscillations: Observations and predictions, in: 15th Int. Symp. on Transportation and Traffic Theory, Elsevier, 2002, pp. 653–674.
- [34] B. Coifman, S. Krishnamurthy, X. Wang, Lane-change maneuvers consuming freeway capacity, in: *Traffic and Granular Flow 03*, Springer Berlin Heidelberg, 2005, pp. 3–14.
- [35] S. Ahn, C. M. J., Freeway traffic oscillations and vehicle lane-change maneuvers, in: 17Th Int. Symp. on Transportation and Traffic Theory, Elsevier, 2007, pp. 691–710.
- [36] Z. Zheng, S. Ahn, D. Chen, J. Laval, Freeway traffic oscillations: Microscopic analysis of formations and propagations using wavelet transform, *Trans. Res. Part B* 45 (9) (2011) 1378–1388.
- [37] X. Litrico, V. Fromion, *Modeling and control of hydrosystems*, Springer, 2009.
- [38] X. Litrico, V. Fromion, H-infinity control of an irrigation canal pool with a mixed control politics, *IEEE Transactions on Control Systems Technology* 14 (1) (2006) 99–111.
- [39] T. W. Sturm, *Open channel hydraulics*, McGraw-Hill, 2001.
- [40] A. Hofleitner, C. Claudel, A. Bayen, Reconstruction of boundary conditions from internal conditions using viability theory, in: *American Control Conference*, IEEE, 2012, pp. 640–645.
- [41] L. Edie, P. of New York Authority, Discussion of Traffic Stream Measurements and Definitions, Port of New York Authority, 1963.